How to cite: Angew. Chem. Int. Ed. 2024, e202401323
doi.org/10.1002/anie.202401323

Molecular Electronics Hot Paper

Connections to the Electrodes Control the Transport Mechanism in Single-Molecule Transistors

Zhixin Chen, Steffen L. Woltering, Bart Limburg, Ming-Yee Tsang, Jonathan Baugh, G. Andrew D. Briggs, Jan A. Mol, Harry L. Anderson,* and James. O. Thomas**

Abstract: When designing a molecular electronic device for a specific function, it is necessary to control whether the charge-transport mechanism is phase-coherent transmission or particle-like hopping. Here we report a systematic study of charge transport through single zinc-porphyrin molecules embedded in graphene nanogaps to form transistors, and show that the transport mechanism depends on the chemistry of the molecule–electrode interfaces. We show that van der Waals interactions between molecular anchoring groups and graphene yield transport characteristic of Coulomb blockade with incoherent sequential hopping, whereas covalent molecule–electrode amide bonds give intermediately or strongly coupled single-molecule devices that display coherent transmission. These findings demonstrate the importance of interfacial engineering in molecular electronic circuits.

[*] Dr. Z. Chen, Dr. S. L. Woltering, Dr. M.-Y. Tsang, Prof. Dr. G. A. D. Briggs, Dr. J. O. Thomas
Department of Materials
University of Oxford
16 Parks Road, Oxford OX1 3PH, UK
E-mail: zhixin.chen@materials.ox.ac.uk

Dr. S. L. Woltering, Dr. B. Limburg, Prof. Dr. H. L. Anderson
Department of Chemistry
University of Oxford
Chemistry Research Laboratory, Oxford OX1 3TA, UK
E-mail: harry.anderson@chem.ox.ac.uk

Prof. Dr. J. Baugh
Institute for Quantum Computing
University of Waterloo
200 University Avenue West, N2 L 3G1 Waterloo, ON, Canada

Prof. Dr. J. A. Mol, Dr. J. O. Thomas
School of Physical and Chemical Sciences
Queen Mary University of London
Mile End Road, London E1 4NS, UK
E-mail: j.o.thomas@qmul.ac.uk

Introduction

Electrons display wave–particle duality.[1] In most cases it is helpful to consider the flow of electrons through a molecule by thinking in terms of either a semi-classical particle model or a coherent-wave model. In the particle model, the molecule is considered as a redox center and an electron is transported through the molecular junction by a sequence of electron-transfer steps, e.g., from an occupied molecular orbital (i.e., the HOMO) to one electrode, and then from the other electrode to the oxidized molecule (Figure 1a).[2] Localization of charge on the molecule between tunnelling events leads to on-site Coulomb energy and electron-vibrational interactions. The resulting electron-transfer mechanism is known as hopping or sequential tunnelling.[3] In the wave model, non-interacting electrons scatter through a molecular junction with energy-dependent transmission probabilities that are influenced by the phase properties of the frontier molecular orbitals (Figure 1b).[4] Marcus theory and Landauer–Büttiker frameworks have been used extensively to model particle-like and wave-like transmission in molecular junctions, respectively. Although formulated independently, these two approaches arise as limiting cases of a unified quantum model that accounts for molecule–electrode coupling, vibrational dynamics, and the measurement temperature.[5]

Experimental control over the nature of electron transport through a junction is needed both to study molecular quantum transport on a fundamental level and to fabricate devices with specific functions. For example, if single-molecule devices are to be used as a test-bed for studying phenomena such as electron–vibration coupling,[6] electron correlation,[7] or spin-dependent transport,[8] then individual contributions of quantum states to transport need to be resolved, and weaker coupling is required. On the other hand, proof-of-principle molecular electronic devices designed for applications such as low-power computing often seek to exploit quantum-interference effects, for which coherent wave-like transmission is essential.[9]

The principal device parameters that define the electron-transport mechanism (at a fixed temperature) are the molecule-electrode coupling (Γ), and the level alignment, ε_0. The former is largely determined by chemical bonding between the molecule and the source and drain electrodes, and thus can be controlled through molecular design and interface engineering. The particle model is useful when molecule–electrode coupling is weak (small Γ), since off-resonant transport is suppressed by electron–electron repul-

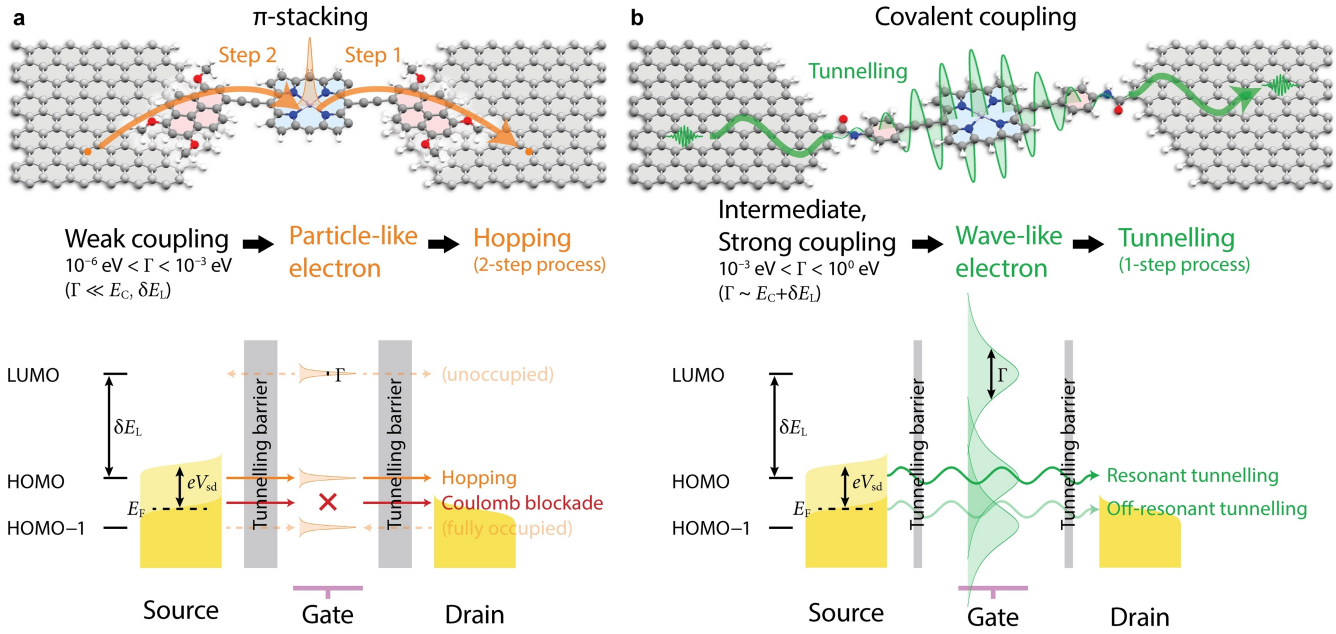

Figure 1. Transport mechanisms. (a) Schematic representation of two-step sequential hopping (electron transfer) through a weakly coupled molecular device, exhibiting the particle nature of an electron. (b) Schematic representation of one-step coherent tunnelling through broadened molecular orbitals for electron transmission through intermediately or strongly coupled molecular devices, exhibiting the wave nature of the electron. Solubilizing groups on porphyrins and pyrenes are omitted for clarity. Γ represents electronic coupling, E_c represents charging energy, δE_L represents level spacing, and $E_c+\delta E_L$ represents addition energy.

sion (Coulomb blockade) and on-resonance transport occurs by sequential electron-transfer steps (Figure 1a). On the other hand, the wave model is useful when strong hybridization between molecular and electrode states yields a large Γ and transport that is fast on the timescale of vibrational dynamics, leading to elastic electron transmission on and off resonance (Figure 1b). In intermediately coupled cases, the distinction between these pictures breaks down, with off-resonant transmission and charge localization due to Coulomb blockade coexisting in the transport spectrum of the same device.[10]

Previously, we investigated charge transport through molecular devices constructed by π-stacking a porphyrin derivative onto electroburnt graphene source and drain electrodes using polycyclic aromatic hydrocarbon anchoring groups.[2a,7a,8b,11] Other studies have explored covalently bonding different molecular cores to nanometer-spaced graphene electrodes using amide coupling.[9a,12] Between these coupling strategies a mix of sequential transport,[2a,12a,13] intermediate coupling,[6a] and phase-coherent transmission[10] have been observed in small numbers of devices. In this work, we present a systematic experimental study of the effect of molecule–electrode chemistry on a larger set of graphene-based single-molecule devices (~1200 devices) fabricated with the same porphyrin core in a three-terminal transistor geometry (Figure 2a–c). We demonstrate a correlation between Γ and the nature of the interfaces and show the effect on the charge-transport mechanism, providing insight into challenges and design strategies for fabricating functional molecular devices.

Results and Discussion

The device architecture, shown schematically in Figure 2a, has been described in detail previously.[14] Graphene is used as the source- and drain-electrode material, because its two-dimensional nature gives it a weaker screening effect on the gate electric field than that of 3D metallic electrodes.[11a,15] The combination of graphene and a thin, high-κ gate dielectric (10 nm HfO_2) means the molecular energy levels can be modulated over a range of typically of >1 eV. The exact value is device dependent, and given by $\alpha_g V_g$, where α_g is the coupling between gate voltage and molecular levels, and V_g is the gate voltage. For this architecture, α_g is ~0.1–0.5 eV/V and V_g is typically limited to ~±4–5 V before dielectric breakdown.[2b] Therefore, in such a transistor geometry, the level alignment can be shifted by the gate potential, $\varepsilon_0=\varepsilon-\mu_F-\alpha_g V_g$, (ε is the energy of a molecular energy level and μ_F is the Fermi level of the electrodes), modulating transport between on-resonance or off-resonance (i.e., whether the molecular level is within the bias window generated by applying a source–drain voltage V_{sd}).

The graphene bowtie shape (Figure 2a) is fabricated by a combination of electron-beam lithography and oxygen plasma, and formed into a pair of nanometer-spaced graphene source and drain electrodes (a graphene nanogap) by feedback-controlled electroburning.[14] Current maps (I_{sd} as a function of source-drain voltage, V_{sd}, and V_g) were measured for each device that was successfully electroburnt to a resistance of 1 GΩ prior to molecular connection. This electroburning procedure gives gap widths, viz., the spacing

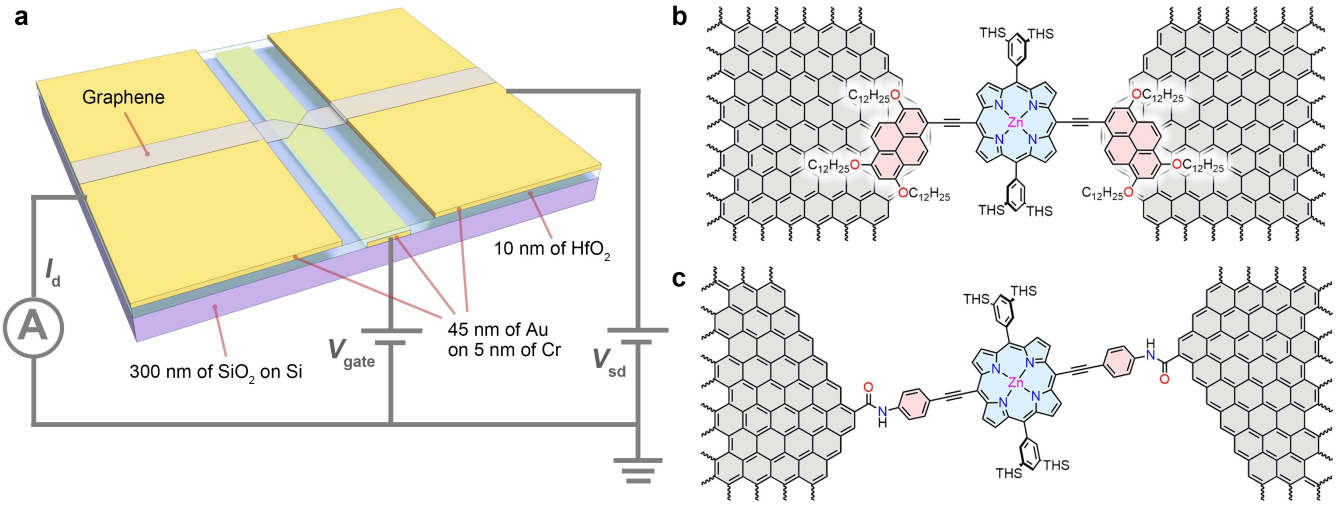

Figure 2. Three-terminal device structure. (a) Schematic of the device architecture. A local gate electrode (yellow rectangular strip in the middle) runs under a 10 nm thick layer of HfO_2 (transparent light blue); the rectangular areas (yellow) at either side are gold and contact the bowtie-shaped graphene constriction (grey) that is electroburnt into nanometer-spaced source and drain electrodes, i.e., a graphene nanogap. Scheme displaying π-stacking (b) and amide coupling (c) a zinc-porphyrin core across a graphene nanogap. THS = trihexylsilyl, the *bis*-3,5-(trihexylsilyl)phenyl groups are for solubility.

between graphene source and drain electrodes, of 1.0–2.5 nm.[11a]

Porphyrin derivatives are commonly chosen molecular cores for single-molecule transport studies because of their modular chemistry and large π-conjugated systems that give small level spacings and small reorganization energies for electron transfer.[16] To generate single-molecule devices with a π-stacking connection, the porphyrin precursor is functionalized with polycyclic aromatic groups, e.g., pyrenes (shown in Figures 1a and 2b), hexabenzocoronenes or tetrabenzofluorenes, and then dropcast from solution onto the graphene nanogaps. The synthesis of these compounds and detailed descriptions of the π-stacking graphene–porphyrin devices have been reported previously.[11a]

For amide coupling, we synthesized two compounds, ***p*-ZnP** and ***m*-ZnP** (both shown in Scheme S1–1), which have either a *para*- or *meta*- arrangement of the amine anchoring group and the porphyrin macrocycle around connecting phenyl rings, by Sonogashira coupling a dibromo-zinc-porphyrin precursor with 4-ethynylaniline and 3-ethynylaniline, respectively. The mechanism of electroburning of graphene in air involves oxidation,[17] and the nanogap edges are decorated with oxygen-containing functional groups. Previous research has shown that it is possible to couple a molecule across graphene-nanogap electrodes by immersing the devices into a solution of amine-functionalized molecules under amide-coupling conditions, suggesting that the edge groups include carboxylic acids.[9a,12] Chips containing graphene nanogaps were immersed in dichloromethane: triethylamine (1:1) solutions containing either ***m*-ZnP** or ***p*-ZnP** and an amide coupling reagent (DIC, HATU or EDIC) for 48 hours, then washed and dried, to generate covalently coupled single-molecule devices (shown in Figures 1b and 2c). More details of coupling and control experiments are given in Supporting Information (Figures S5 and S6, respectively).

Current–voltage maps (I_{sd} vs. V_{sd} and V_g) were taken before and after the molecular connection for 555 amide-coupled devices, and for 666 π-stacked devices. To make initial comparisons between the large numbers of devices, we plotted the zero-bias conductance (at $V_g = 0$ V) of each device before and after the molecular connection (Figures 3a and 3b). There is a wide spread of values, but a notable difference between the two datasets is that graphene nanogaps subjected to amide-coupling showed significantly more devices with a large increase in conductance after the molecular connection, with a cluster of devices in the top-left of Figure 3b. Overall, 5.6 ± 1.9 % of devices subjected to amide coupling displayed a hundred-fold increase in conductance after molecular connection, compared to 1.4 ± 1.0 % of π-stacking devices, which is a statistically significant difference (p-value = 3×10^{-5}; see Supporting Information for p-value calculation). The result for π-stacking is similar to control experiments where the devices were immersed in a solution of just ***p*-ZnP**, or just with the coupling reagent (127 devices in total), as shown in Supporting Information.

Zero-bias conductance and I_{sd}–V_{sd} measurements at zero gate voltage can elucidate trends but are of limited use for molecular devices. For strongly coupled devices, close alignment between the graphene Fermi level and nearest orbital is not necessary to observe a conductance increase, as current can flow efficiently by off-resonant transmission through lifetime-broadened molecular orbitals (i.e., that have a FWHM of Γ). If molecule–electrode coupling is sufficiently weak, however, so that the transport mechanism is first-order sequential tunnelling, then current only flows when a molecular energy level is on resonance; otherwise it is suppressed by a Coulomb blockade. Consequently, if there is no transition within k_BT of the Fermi levels of the

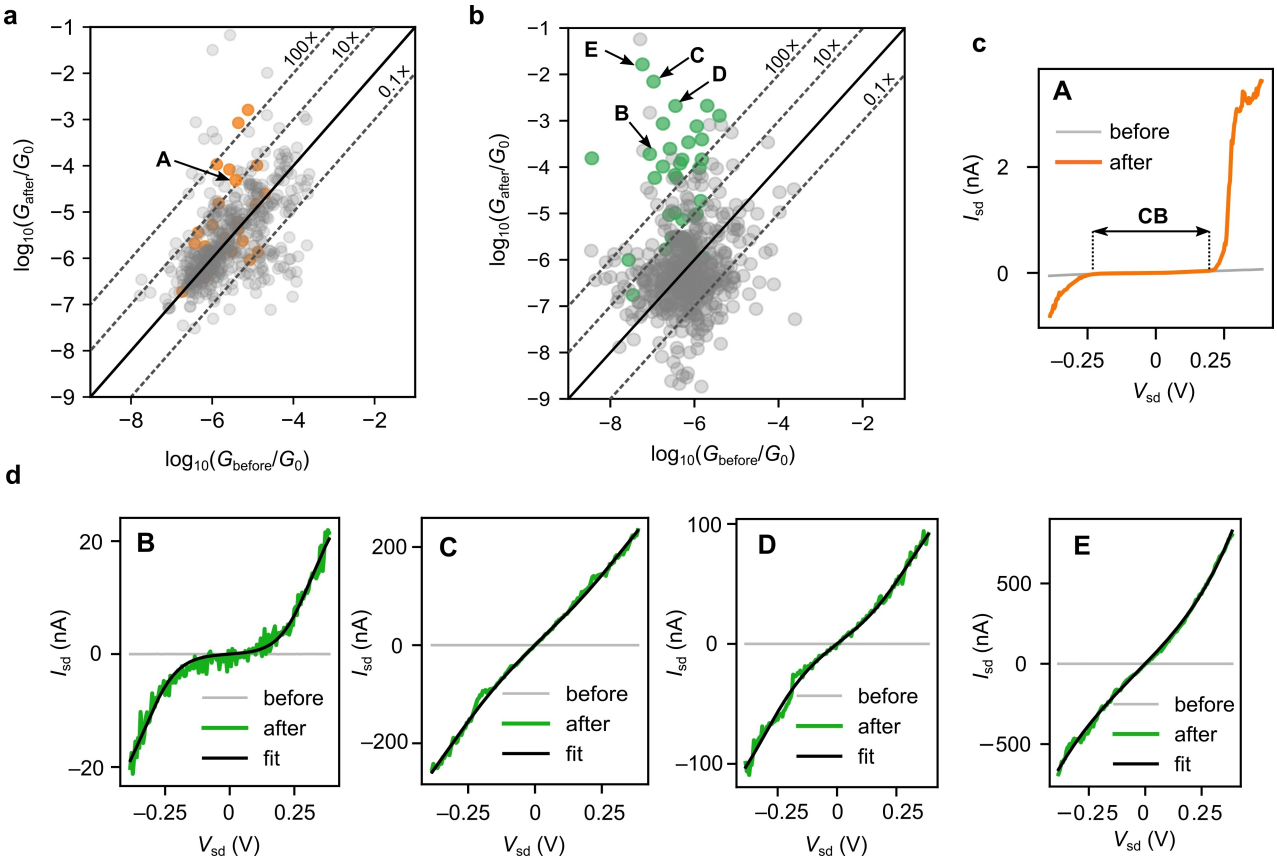

Figure 3. Device comparisons. Scatter plots of zero-bias conductance before and after molecular connection by (a) π-stacking[11a] or (b) amide-coupling anchoring chemistry. Each marker represents a single device, with the conductance before connection as the *x*-value, and conductance after as the *y*-value. Devices identified as molecular devices from full stability-diagram measurements are highlighted in orange (π-stacking) or green (amide coupling). The solid diagonal lines represent devices that do not change conductance after the coupling, and dashed lines are labelled with the factor that conductance changes by after coupling. (c) Before and after I_{sd}–V_{sd} measurements of device **A** (indicated by the arrow on panel a), which is a π-stacked device that displays weak-coupling and Coulomb blockade (CB). (d) Before and after I_{sd}–V_{sd} measurements of amide-coupling devices (**B**–**E**) with fits to Equations (1–4) in the main text. Fitting parameters: **B**: $\Gamma = 1.6$ meV, $\varepsilon_0 = 0.15$ eV, $\alpha_s = 0.48$, **C**: $\Gamma = 240$ meV, $\varepsilon_0 = 0.16$ eV, $\alpha_s = 0.48$, **D**: $\Gamma = 120$ meV, $\varepsilon_0 = 0.14$ eV, $\alpha_s = 0.54$, **E**: Γ 250 meV, $\varepsilon_0 = 0.31$ eV, $\alpha_s = 0.56$. Amide coupling device measurements were done at room temperature. **B**–**D** are ***p*-ZnP** devices and **E** is a ***m*-ZnP** device.

graphene electrodes at $V_g = 0$ V, then no change in zero-bias conductance is expected, even if the nanogap is bridged by a molecule. An example of this is shown in Figure 3c, where a π-stacking molecular device (device **A**, the anchoring group is shown in Figure 2b) shows little current increase until the bias window is large enough to lift the Coulomb blockade at V_{sd}~250 mV.

Various methods have been used to define the 'device yield' in studies of static single-molecule junctions. The simplest method is to classify a device as 'molecular' if there is an increase in current after a coupling procedure, through comparison of I_{sd}–V_{sd} curves. If this over-simplified method is applied to the devices studied in this work, all the devices above the solid diagonal line ($G_{after} > G_{before}$) in Figure 3a and 3b would be counted (these are not those highlighted in Figure 3) giving yields of 49.3 ± 3.4 % (274/555) for amide coupling, 51.2 ± 3.2 % (341/666) for π-stacking, but also 48.8 ± 7.2 % (62/127) for the control experiment. This result is perhaps unsurprising, as the exponential dependence of tunnelling current on barrier height and width means that small fluctuations at the atomic level that may occur during the coupling chemistry will lead to measurable changes in tunnelling current,[18] with half of these random fluctuations increasing device conductance. Therefore, to classify any particular junction as a 'molecular device' and obtain a yield we chose to compare each pair of 2D maps of tunnelling current as a function of V_{sd} and V_g before and after molecular connection.[11a] The points highlighted by green or orange markers in Figures 3a and 3b are those identified as molecular devices from making these comparisons. Devices were classified using an unsupervised algorithm for data selection (see details in Supporting Information Section 4), based on whether transport features (viz., features in G_{sd}–V_g, not necessarily at $V_g = 0$ V) only appeared after molecular deposition. This comparative approach is necessary because residual carbon quantum dots can produce resonant tunnelling regions prior to molecular deposition, as discussed previously.[11a] The before and after maps measured at room temperature are given in the Supporting Information (Figures S8–S12) for all amide-coupling devices, and for

the π-stacking devices they are given in Ref. [11a]. The conductances of our molecular devices are distributed over several orders of magnitude. This distribution is the result of different atomic-scale structures of electrodes and bonding geometries from device to device, and is consistent with high-quality STM-break-junction (BJ) results.[9b,19] The average value of the conductance is also close to the result of a similar molecular core with thiol (thioacetate) anchors measured on STM-BJ.[20] Overall, we estimate the device yield as 5.8 % ± 1.9 % (32/555) for amide coupling and 3.9 % ± 1.2 % (26/666) for π-stacking, respectively, using this method.

The orange markers that represent π-stacked devices in Figure 3a are not shifted much from the junctions without molecules. In contrast, the amide-coupled devices often have an increase in zero-bias conductance at $V_g = 0$ V by more than two orders of magnitude, as indicated by the cluster of green markers in the upper left of Figure 3b. Four examples of I_{sd}–V_{sd} curves for amide-coupled ***p*-ZnP** devices are given in Figure 3d (device **B** has slightly different geometry to Figure 2a as reported in our recent research[11]). Results from other devices are included in the Supporting Information (Figures S13–S15). The large increases in zero-bias conductance after amide coupling suggest that these particular amide-coupled devices are not in the weak-coupling regime. Off-resonant transmission then contributes to the tunnelling current, reducing the importance of energy-level alignment for zero-bias conductance. Stronger coupling would also be consistent with the large device currents measured (Figure 3d).

To draw more robust conclusions about the tunnelling mechanisms, we wire-bonded devices and measured again at ~77 K to reduce thermal noise. The conductance map and zero-bias gate trace of device **A** (π-stacking) are shown in Figures 4a and 4c, respectively. They display Coulomb-blockade behavior characteristic of a weakly coupled molecular device. There is high conductance when a molecular energy level lies within the bias window between the electrode potentials, where resonant sequential tunnelling between many-body charge states of the molecule is permitted, and conductance is suppressed in the off-resonant, Coulomb-blocked regions. The zero-bias conductance peaks at $V_g = -1$ V and $V_g = -4$ V correspond to the alignment of the first oxidation ($\mu_{N\text{-}1/N}$) and second oxidations ($\mu_{N\text{-}2/N\text{-}1}$) of the molecule with the chemical potentials of the electrodes. Outside these thermally broadened peaks, the conductance is at the noise level of the measurement. The diamond-shaped regions of conductance suppression (Coulomb diamonds) can be assigned molecular charge (redox) states *N*, *N*-1, and *N*-2, where *N* is the number of electrons on the molecule in the neutral state. The edges of Coulomb diamonds are sharp, indicating strong charge localization and a molecular oxidation state that is well-defined across the conductance map.

The conductance maps of the amide-coupling devices (Figure 4b) are very different from those of π-stacking devices. There is high conductance (~10^{-3} G_0) across most of the V_g range, and Coulomb diamonds are barely distinguishable, indicating an off-resonant transport mechanism through molecular orbitals that are strongly hybridized with the graphene, rather than sequential transport and associ-

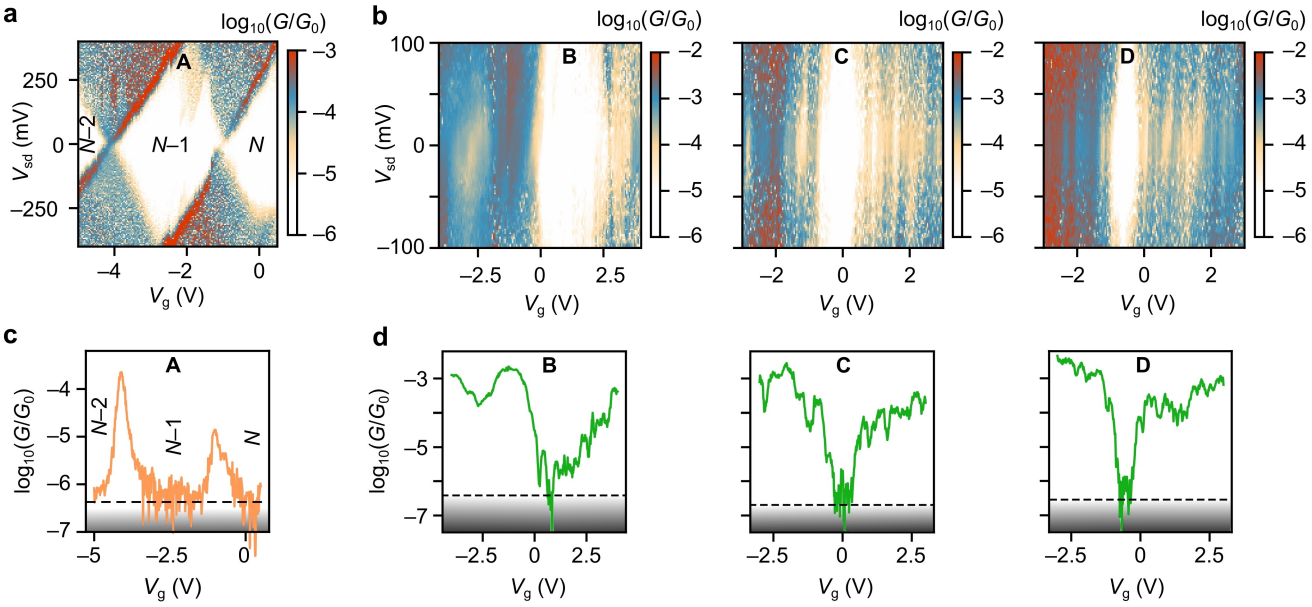

Figure 4. Differential conductance characteristics. (a) Differential conductance maps for (a) π-stacking device **A** and (b) amide-coupling devices **B**–**D**. (c,d) Zero-bias conductance gate traces for the devices. Coulomb blockade is observed for device **A** and molecular charge states (*N*-2, *N*-1, *N*) can be assigned. For devices **B**–**D**, an anti-resonance feature is observed which reduces the conductance to down to the noise level of the measurements (horizontal dashed lines) over a gate range close to $V_g = 0$ V. The noise level is around $10^{-(6.5\text{–}7.0)}$ G_0, and depends on the specific measurement set-up and current amplifier settings. The measurement temperature is 77 K (device **A**) or 80 K (devices **B**–**D**). A low-temperature conductance gate trace of device **E** is shown in Figure S7 of the Supporting Information.

ated charge localization. These observations confirm the indications in Figure 3 that amide-coupled devices have stronger molecule–electrode coupling. This trend contradicts a theoretical study of these two anchoring strategies that predicted only moderate differences in conductance and higher conductance for devices using pyrene anchoring groups rather than amide bonds.[21] If the calculations are correct, then the discrepancy may be the result of only partial overlap of planar anchoring groups with graphene, or residual adsorbed contamination from either atmosphere or fabrication processing that prevents a close anchor–graphene π–π interaction.

It has been reported, and research has shown in a junction with gold electrodes,[22] that hybridization of molecular orbitals with the electrodes in the strong coupling regime should broaden the orbital resonances to the extent that conductance becomes almost independent of V_g. Instead, we observe an anti-resonance in the conductance around V_g~0 V where the current reduces to the noise level, as well as some smaller G–V_g fluctuations (shown in Figure 4d). Our recent study,[9a] along with theoretical work,[23] showed that the conductance minima around V_g = 0 V are a result of destructive quantum interference at the graphene–molecule interface, which is why the minima appear for both precursor isomers. Suppressions in the local density of states at the edge atoms of graphene reduce the device transmission around the Fermi level, causing the anti-resonance features. The smaller G_{sd}–V_g fluctuations are harder to assign, but could result from further interference effects,[10] density-of-states fluctuations in graphene,[24] additional molecular orbitals contributing to transport, or vibrational effects.

In order to correlate the observed behavior with the level alignment and molecule–electrode coupling, we use the following expression for first-order transport processes through a single-level:[2a]

$$I_{sd} = \frac{\gamma_L \bar{\gamma}_R - \gamma_R \bar{\gamma}_L}{\gamma_L + \gamma_R + \bar{\gamma}_L + \bar{\gamma}_R}, \quad (1)$$

where γ_l and $\bar{\gamma}_l$ denote the rates of tunnelling to and from the molecule respectively, at each electrode (l = L/R). The rates are given by

$$\gamma_l = \Gamma_l \int f_l(\varepsilon) k(\varepsilon)\, d\varepsilon, \quad (2)$$

$$\overline{\gamma_l} = \Gamma_l \int [1 - f_l(\varepsilon)] \bar{k}(\varepsilon)\, d\varepsilon, \quad (3)$$

where Γ_l is the molecule–electrode coupling, and $f_l(\varepsilon)$ is the Fermi–Dirac distribution at electrode l. Statistical prefactors that result from spin degeneracy can be included in the equations of the rates, which is necessary in the weakly coupled limit.[25] The molecular density of states k are given by:

$$k = \mathrm{Re} \int_0^\infty e^{\sigma i(\varepsilon - \varepsilon_0)t/\hbar} e^{-\Gamma t/\hbar} B(t)\, dt, \quad (4)$$

where $\Gamma/\hbar$ is the lifetime of the electronic state. $B(t)$ is the phononic correlation function, a time-dependent Franck–Condon factor that describes the vibrational dynamics that accompanies electron tunnelling. For k and $\bar{k}$ the factor σ is +1 or −1, respectively.

Following previous work,[2a,5,7a] the phonon-correlation function $B(t)$ is generated from DFT-calculated electron–phonon coupling constants. For π-stacking devices, ε_0 is calculated as the product of gate voltage of the nearest Coulomb peak and the gate coupling α_g (which is in turn calculated from the slopes of the Coulomb diamonds).[26] The couplings, Γ ($=\Gamma_L+\Gamma_R$) are then fitting parameters to I–V traces on these resonances.[2a] For the amide-coupling devices there is no clear Coulomb peak, so ε_0 and the molecule–electrode couplings are fitting parameters.

The fits to equation 1 for devices **B**–**E** are shown on the respective I–V curves in Figure 3d, and the remaining devices are in Supplementary Figures S13–S15. In Figure 5, we plot the (ε_0, Γ) pairs for both sets of devices. The electronic couplings of π-stacking molecular devices are in the range 10^{-6}–10^{-2} eV, whereas for amide-coupling devices the values are higher, mainly between 10^{-3} and 10^{0} eV. Differences in the magnitude in electronic coupling therefore correlate with the different transport mechanisms observed experimentally in Figure 4. It is common to classify the transport regime (strong/intermediate/weak) through the ratio $\Gamma/\delta E_L$, where δE_L represents the energy spacings of the molecule. If we take δE_L to be the energy differences between charge states (addition energies, E_{add}), we can read them directly from a stability diagram[2b] ($E_{add}(N-1)$ ~400 meV for device **A**) or approximate them from solution-phase cyclic voltammetry (1.7 eV between the first oxidation and reduction wave, and 0.2–0.5 eV for subsequent spacings for molecule in device **A**).[11a] Our calculated

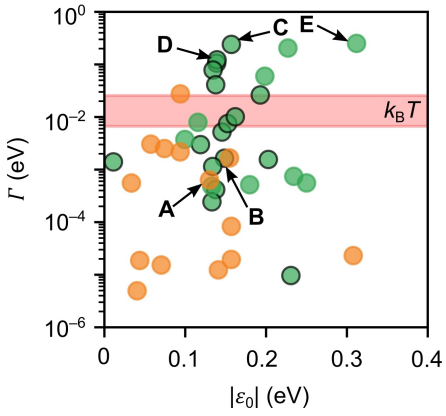

Figure 5. Transport parameters. Scatter plots of level alignment and electronic coupling for amide-coupling (green markers, black outline for ***p*-ZnP**, green outline for ***m*-ZnP**) and π-stacking (orange markers) devices. The red band represents the thermal-energy, k_BT with upper and lower limits corresponding to 298 K and 77 K, respectively.

ratios of $\Gamma/\delta E_L$ are broadly in line with definitions of weak coupling ($\Gamma/\delta E_L < 0.1$) for π-stacking, and intermediate coupling ($0.1 < \Gamma/\delta E_L < 1$) for amide coupling. If, alternatively, we take δE_L to be the orbital spacings in an isolated molecule (calculated by DFT), then similar ratios are found. For comparison with cyclic voltammetry or, especially DFT calculations, some device-dependent renormalization of the values is expected.

As we have observed above, the charge-transport mechanism also depends on the vibrational effects associated with electron transport. In Figure 6 we plot the effects of both the vibrational correlation and the finite lifetimes of electronic states involved in transport in the time and energy domains.[27] For device **A** (π-stacking, $\Gamma = 0.6$ meV), the relative timescales of vibrational dynamics and the finite lifetime are similar, leading to inelastic processes contributing to the energy-dependence of k and $\bar{k}$. For device **C** (amide coupling, Γ~240 meV), however, the short excited-state lifetime dominates the dynamics. In this limit, $B(t)e^{-\Gamma t/\hbar} \sim e^{-\Gamma t/\hbar}$ (seen in Figure 6b); the energy dependence has the form of a Lorentzian broadened by Γ; and the equations above reduce to the non-interacting Landauer description (commonly known as the single-level model).[5]

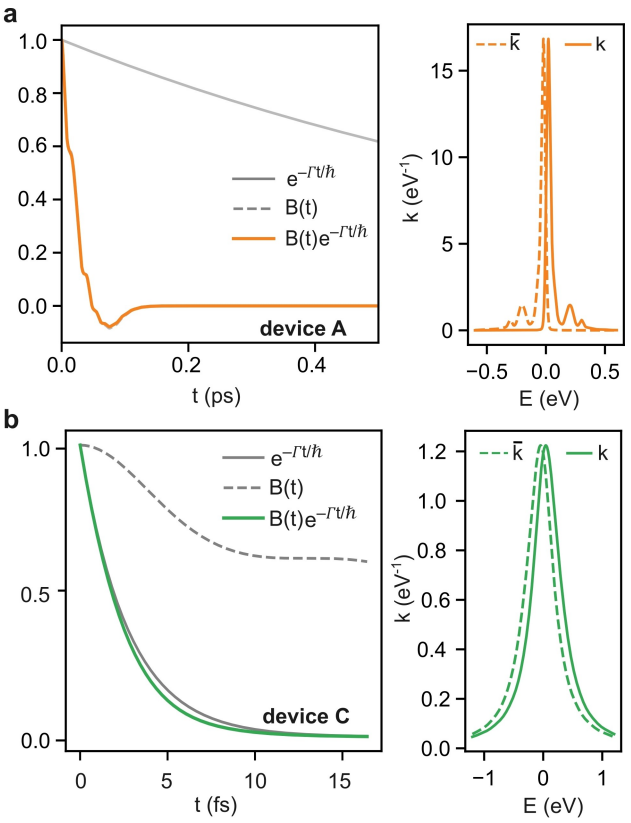

Figure 6. Time- and energy-dependence. Calculated phonon-correlation functions and lifetime-broadening of (a) device **A** and (b) device **C**, using the parameters from the fits to equations 1–3 and DFT-calculated electron–phonon couplings. The vibrational dynamics for weakly-coupled device **A** ($\Gamma = 0.6$ meV) result in a structured energy dependence of the molecular densities of states, k and $\bar{k}$. For device **C** ($\Gamma = 240$ meV), dynamics are dominated by lifetime-broadening and k and $\bar{k}$ are Lorentzian functions broadened by Γ, equivalent to the energy dependence of transmission for the single-level model. The electron–phonon correlation functions are calculated at 77 K.

For strongly coupled devices, there have been numerous experimental and theoretical studies that have demonstrated quantum-interference effects in molecular conductance measurements, confirming that transport is, at least partly, phase-coherent.[28] For devices that display Coulomb blockade, transport is not *a priori* incoherent, as electronic interferometric measurements have shown that transport through Coulomb peaks can be phase-coherent.[29] As shown in Figure 6a, however, when the timescales ($\hbar/\Gamma$) for electron tunnelling are picosecond to nanoseconds (for $\Gamma = 10^{-2}$ to 10^{-6} eV), inelastic vibrational processes are permitted, and these are associated with charge localization and concomitant with decoherence.[11b,30] Therefore, with increasingly weak coupling, transport will become sequential and incoherent.[3b] Overall, the role of vibrational dynamics in charge transport is relatively understudied in the intermediate coupling regime, as it lies outside where either Marcus theory/Frank–Condon physics or Landauer theory would be valid. In these cases, the details of the transport mechanism, and questions regarding the role of quantum coherence in transport, are open and will depend on the interplay between the tunnelling rates and molecular vibrations. Using interfacial chemistry to control the transport regime provides a strategy for addressing these questions.

Conclusion

In this work, we present a systematic study of how different molecule–electrode connections affect charge-transport properties of graphene-based zinc-porphyrin devices. For covalent molecule–electrode links, couplings vary over several orders of magnitude, but often exceed 10 meV, resulting in phase-coherent transmission. For π-stacking, couplings are in the μeV–meV range, and transport is characterized by Coulomb blockade and sequential tunnelling that is likely to be incoherent. The results demonstrate how changing the chemistry of the connection to the electrodes can be used to access different regimes of electron transport through a molecular device, which is a prerequisite for designing functional devices that harness interference effects or studying the influence of individual quantum vibrational or spin states on conduction. Furthermore, we have highlighted challenges in the field, such as the need for both a robust definition of device yield, and device-to-device variability. The methods we present here give dynamic information on single-molecule devices and shed new light on the fundamentals of transport mechanisms.

Supporting Information

Supporting Information is available from the Wiley Online Library or from the author. The authors have cited additional references within the Supporting Information.

Acknowledgements

The authors would like to acknowledge the use of the University of Oxford Advanced Research Computing (ARC) facility in carrying out part of this work (https://doi.org/10.5281/zenodo.22558). The work was supported by the EPSRC (grants EP/N017188/1 QuEEN and EP/R029229/1 NS2NF) and the ERC (ERC-AdG-885606 ARO-MAT). JAM acknowledges funding from the Royal Academy of Engineering and a UKRI Future Leaders Fellowship, Grant No. MR/S032541/1.

Conflict of Interest

The authors declare no conflict of interest.

Data Availability Statement

The data that support the findings of this study are available from the corresponding author upon reasonable request.

Keywords: single-molecule transistor · charge transport · vibrational coupling · electron transfer · interface engineering

[1] C. Jnsson, *Z. Phys.* **1961**, *161*, 454–474.
[2] a) J. O. Thomas, B. Limburg, J. K. Sowa, K. Willick, J. Baugh, G. A. D. Briggs, E. M. Gauger, H. L. Anderson, J. A. Mol, *Nat. Commun.* **2019**, *10*, 4628; b) M. L. Perrin, E. Burzuri, H. S. van der Zant, *Chem. Soc. Rev.* **2015**, *44*, 902–919.
[3] a) P. Gehring, J. M. Thijssen, H. S. J. van der Zant, *Nat. Rev. Phys.* **2019**, *1*, 381–396; b) M. Galperin, M. A. Ratner, A. Nitzan, *J. Condens. Matter Phys.* **2007**, *19*, 103201.
[4] a) G. C. Solomon, D. Q. Andrews, T. Hansen, R. H. Goldsmith, M. R. Wasielewski, R. P. Van Duyne, M. A. Ratner, *J. Chem. Phys.* **2008**, *129*, 054701; b) K. Yoshizawa, *Acc. Chem. Res.* **2012**, *45*, 1612–1621.
[5] J. K. Sowa, J. A. Mol, G. A. D. Briggs, E. M. Gauger, *J. Chem. Phys.* **2018**, *149*, 154112.
[6] a) E. Burzuri, J. O. Island, R. Diaz-Torres, A. Fursina, A. Gonzalez-Campo, O. Roubeau, S. J. Teat, N. Aliaga-Alcalde, E. Ruiz, H. S. van der Zant, *ACS Nano* **2016**, *10*, 2521–2527; b) E. A. Osorio, K. O'Neill, N. Stuhr-Hansen, O. F. Nielsen, T. Bjornholm, H. S. J. van der Zant, *Adv. Mater.* **2007**, *19*, 281–285.
[7] a) J. O. Thomas, J. K. Sowa, B. Limburg, X. Bian, C. Evangeli, J. L. Swett, S. Tewari, J. Baugh, G. C. Schatz, G. A. D. Briggs, H. L. Anderson, J. A. Mol, *Chem. Sci.* **2021**, *12*, 11121–11129; b) S. Kubatkin, A. Danilov, M. Hjort, J. Cornil, J. L. Bredas, N. Stuhr-Hansen, P. Hedegard, T. Bjornholm, *Nature* **2003**, *425*, 698–701.
[8] a) J. de Bruijckere, P. Gehring, M. Palacios-Corella, M. Clemente-Leon, E. Coronado, J. Paaske, P. Hedegard, H. S. J. van der Zant, *Phys. Rev. Lett.* **2019**, *122*, 197701; b) T. Pei, J. O. Thomas, S. Sopp, M. Y. Tsang, N. Dotti, J. Baugh, N. F. Chilton, S. Cardona-Serra, A. Gaita-Arino, H. L. Anderson, L. Bogani, *Nat. Commun.* **2022**, *13*, 4506; c) R. Gaudenzi, J. de Bruijckere, D. Reta, I. P. R. Moreira, C. Rovira, J. Veciana, H. S. J. van der Zant, E. Burzuri, *ACS Nano* **2017**, *11*, 5879–5883; d) H. B. Heersche, Z. de Groot, J. A. Folk, H. S. van der Zant, C. Romeike, M. R. Wegewijs, L. Zobbi, D. Barreca, E. Tondello, A. Cornia, *Phys. Rev. Lett.* **2006**, *96*, 206801.
[9] a) Z. Chen, I. M. Grace, S. L. Woltering, L. Chen, A. Gee, J. Baugh, G. A. D. Briggs, L. Bogani, J. A. Mol, C. J. Lambert, H. L. Anderson, J. O. Thomas, *Nat. Nanotechnol.* **2024**, DOI: 10.1038/s41565-024-01633-1; b) J. Liu, X. Huang, F. Wang, W. Hong, *Acc. Chem. Res.* **2019**, *52*, 151–160; c) Y. Li, J. A. Mol, S. C. Benjamin, G. A. Briggs, *Sci. Rep.* **2016**, *6*, 33686.
[10] Z. Chen, J. R. Deng, S. Hou, X. Bian, J. L. Swett, Q. Wu, J. Baugh, L. Bogani, G. A. D. Briggs, J. A. Mol, C. J. Lambert, H. L. Anderson, J. O. Thomas, *J. Am. Chem. Soc.* **2023**, *145*, 15265–15274.
[11] a) B. Limburg, J. O. Thomas, G. Holloway, H. Sadeghi, S. Sangtarash, I. C. Y. Hou, J. Cremers, A. Narita, K. Müllen, C. J. Lambert, G. A. D. Briggs, J. A. Mol, H. L. Anderson, *Adv. Funct. Mater.* **2018**, *28*, 1803629; b) X. Bian, Z. Chen, J. K. Sowa, C. Evangeli, B. Limburg, J. L. Swett, J. Baugh, G. A. D. Briggs, H. L. Anderson, J. A. Mol, J. O. Thomas, *Phys. Rev. Lett.* **2022**, *129*, 207702.
[12] a) Q. Xu, G. Scuri, C. Mathewson, P. Kim, C. Nuckolls, D. Bouilly, *Nano Lett.* **2017**, *17*, 5335–5341; b) Y. Cao, S. Dong, S. Liu, L. He, L. Gan, X. Yu, M. L. Steigerwald, X. Wu, Z. Liu, X. Guo, *Angew. Chem. Int. Ed.* **2012**, *51*, 12228–12232.
[13] C. S. Lau, H. Sadeghi, G. Rogers, S. Sangtarash, P. Dallas, K. Porfyrakis, J. Warner, C. J. Lambert, G. A. Briggs, J. A. Mol, *Nano Lett.* **2016**, *16*, 170–176.
[14] a) F. Prins, A. Barreiro, J. W. Ruitenberg, J. S. Seldenthuis, N. Aliaga-Alcalde, L. M. Vandersypen, H. S. van der Zant, *Nano Lett.* **2011**, *11*, 4607–4611; b) C. S. Lau, J. A. Mol, J. H. Warner, G. A. Briggs, *Phys. Chem. Chem. Phys.* **2014**, *16*, 20398–20401.
[15] J. A. Mol, C. S. Lau, W. J. Lewis, H. Sadeghi, C. Roche, A. Cnossen, J. H. Warner, C. J. Lambert, H. L. Anderson, G. A. Briggs, *Nanoscale* **2015**, *7*, 13181–13185.
[16] P. Zwick, D. Dulic, H. S. J. van der Zant, M. Mayor, *Nanoscale* **2021**, *13*, 15500–15525.
[17] M. El Abbassi, L. Posa, P. Makk, C. Nef, K. Thodkar, A. Halbritter, M. Calame, *Nanoscale* **2017**, *9*, 17312–17317.
[18] L. Pósa, Z. Balogh, D. Krisztián, P. Balázs, B. Sánta, R. Furrer, M. Csontos, A. Halbritter, *NPJ 2D Mater. Appl.* **2021**, *5*, 57.
[19] M. S. Hybertsen, L. Venkataraman, *Acc. Chem. Res.* **2016**, *49*, 452–460.
[20] E. Leary, B. Limburg, A. Alanazy, S. Sangtarash, I. Grace, K. Swada, L. J. Esdaile, M. Noori, M. T. Gonzalez, G. Rubio-Bollinger, H. Sadeghi, A. Hodgson, T. N. Agrai, S. J. Higgins, C. J. Lambert, H. L. Anderson, R. J. Nichols, *J. Am. Chem. Soc.* **2018**, *140*, 12877–12883.
[21] H. Sadeghi, S. Sangtarash, C. Lambert, *Nano Lett.* **2017**, *17*, 4611–4618.
[22] a) K. Moth-Poulsen, T. Bjornholm, *Nat. Nanotechnol.* **2009**, *4*, 551–556; b) A. Danilov, S. Kubatkin, S. Kafanov, P. Hedegard, N. Stuhr-Hansen, K. Moth-Poulsen, T. Bjornholm, *Nano Lett.* **2008**, *8*, 1–5.
[23] D. Carrascal, V. M. García-Suárez, J. Ferrer, *Phys. Rev. B* **2012**, *85*, 195434.
[24] P. Gehring, J. K. Sowa, J. Cremers, Q. Wu, H. Sadeghi, Y. Sheng, J. H. Warner, C. J. Lambert, G. A. D. Briggs, J. A. Mol, *ACS Nano* **2017**, *11*, 5325–5331.
[25] B. Limburg, J. O. Thomas, J. K. Sowa, K. Willick, J. Baugh, E. M. Gauger, G. A. D. Briggs, J. A. Mol, H. L. Anderson, *Nanoscale* **2019**, *11*, 14820–14827.
[26] E. A. Osorio, T. Bjornholm, J. M. Lehn, M. Ruben, H. S. van der Zant, *J. Phys. Condens. Matter* **2008**, *20*, 374121.
[27] M. D. Todd, A. Nitzan, M. A. Ratner, J. T. Hupp, *J. Photochem. Photobiol. A* **1994**, *82*, 87–101.
[28] a) J. Bai, A. Daaoub, S. Sangtarash, X. Li, Y. Tang, Q. Zou, H. Sadeghi, S. Liu, X. Huang, Z. Tan, J. Liu, Y. Yang, J. Shi, G. Meszaros, W. Chen, C. Lambert, W. Hong, *Nat. Mater.* **2019**,

18, 364–369; b) Y. Li, M. Buerkle, G. Li, A. Rostamian, H. Wang, Z. Wang, D. R. Bowler, T. Miyazaki, L. Xiang, Y. Asai, G. Zhou, N. Tao, *Nat. Mater.* **2019**, *18*, 357–363; c) M. H. Garner, H. Li, Y. Chen, T. A. Su, Z. Shangguan, D. W. Paley, T. Liu, F. Ng, H. Li, S. Xiao, C. Nuckolls, L. Venkataraman, G. C. Solomon, *Nature* **2018**, *558*, 415–419; d) C. M. Guedon, H. Valkenier, T. Markussen, K. S. Thygesen, J. C. Hummelen, S. J. van der Molen, *Nat. Nanotechnol.* **2012**, *7*, 305–309.

[29] R. Schuster, E. Buks, M. Heiblum, D. Mahalu, V. Umansky, H. Shtrikman, *Nature* **1997**, *385*, 417–420.

[30] H. Bi, C. A. Palma, Y. Gong, K. Stallhofer, M. Nuber, C. Jing, F. Meggendorfer, S. Wen, C. Yam, R. Kienberger, M. Elbing, M. Mayor, H. Iglev, J. V. Barth, J. Reichert, *J. Am. Chem. Soc.* **2020**, *142*, 3384–3391.

Manuscript received: January 19, 2024
Accepted manuscript online: February 27, 2024
Version of record online: ■■, ■■

Research Articles

Molecular Electronics

Z. Chen,* S. L. Woltering, B. Limburg, M.-Y. Tsang, J. Baugh, G. A. D. Briggs, J. A. Mol, H. L. Anderson,* J. O. Thomas* e202401323

Connections to the Electrodes Control the Transport Mechanism in Single-Molecule Transistors

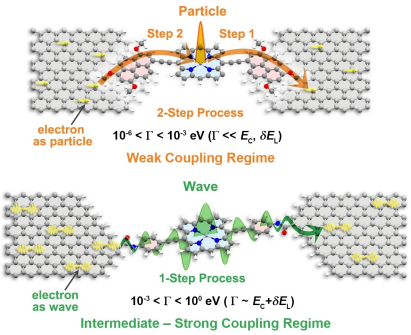

The electron-transport mechanism in a single-molecule transistor can be changed from 'particle-like hopping' to 'wave-like' by changing the chemical structure of the molecule–electrode interface.